Materials Chemistry and Physics 316 (2024) 129103

Contents lists available at ScienceDirect

Materials Chemistry and Physics

journal homepage: www.elsevier.com/locate/matchemphys

Single crystal polarization-orientation Raman spectroscopy of zeolite LTA with confined S_3^- anions - High dielectric constant nanoporous material

Vladimir V. Poborchii [a,*], Vitalii Petranovskii [b], Igor A. Glukhov [c,d], Andrei A. Fotiadi [e,**]

[a] National Institute of Advanced Industrial Science and Technology, Tsukuba, 305-8565, Japan
[b] Centro de Nanociencias y Nanotecnología, Universidad Nacional Autónoma de México, Ensenada, Baja California, Mexico
[c] Lab-STICC (UMR CNRS 6285), École Nationale d'Ingénieurs de Brest, France
[d] Ulyanovsk State University, 42 Leo Tolstoy Street, Ulyanovsk, 432970, Russian Federation
[e] Optoelectronics and Measurement Techniques unit, University of Oulu, Oulu, Finland

ARTICLE INFO

Keywords:
S_3^- anion
LTA single crystal
Raman microscopy
Luminescence
Dielectric constant

ABSTRACT

We apply polarization-orientation Raman spectroscopy, as an alternative to X-ray diffraction, to LTA single crystals containing S_3^- in sodalite cages additionally to S_8 rings in large cavities. The sample was obtained via sulfur vapor adsorption at ~550 °C (LTA-S-550). We show that S_3^- is located in the (110) plane with its 2-fold axis along the LTA 4-fold axis. The anion position suggests strong interaction of its terminal atoms with Na^+ localized in LTA 6-membered rings. The anions display optical absorption band at ~590 nm (2.1 eV) and resonant Raman enhancement. We observe a record-high S_3^- bond-bending mode frequency ~274 cm^{-1} due to a strong bond-angle contraction. This leads to the Fermi resonance of its overtone with the symmetric bond-stretching mode in the frequency range of 544–552 cm^{-1}. An anomalous Raman downshift of the S_3^- bond-stretching modes with a decrease of temperature is observed and attributed to partial compressive stress relaxation. Luminescence band at ~845 nm is observed suggesting considering LTA-S-550 as an interesting light-emitting material. We discuss a role of S_3^- in the high dielectric constant up to ~160 and a possible contribution of the anion to the ion-exchange selectivity to Sr^{2+}/Cs^+ enhancements of LTA with sulfur.

1. Introduction

S_3^- anion radical was observed in the famous pigment ultramarine (sulfur-doped zeolite sodalite (SOD)) [1–7], borosilicate glasses [8,9], liquid solutions of sulfur or its compounds [10–14] and alkali halides [15]. Moreover, it was shown that S_3^- is a dominant form of sulfur in aqueous solutions at elevated temperatures and pressures [16] proving that it is an important component of geological fluids and, therefore, one of the basic molecules of the Earth and Universe. In sense of applications, anionic sulfur species play a crucial role in alkali-metal–sulfur batteries [14,17].

Optical absorption and Raman spectra (OAS and RS) of S_3^- in different environments were intensively studied from 1960s up to now. The S_3^- absorption band at ~600 nm was found to be responsible for the blue (or green in combination with S_2^-) color of ultramarine [1–6,13,18]. Resonant RS, associated with this band, was demonstrated [2,3,13]. Electron paramagnetic resonance (EPR) was also widely used for S_3^- characterization [5,19]. Via sulfur vapor adsorption, S_3^- was obtained in the zeolite LTA with SOD cages and characterized using OAS, RS and EPR [20]. Later S_3^- in LTA was fabricated and examined in a few other works [3,21–24]. Importantly, LTA with sulfur (LTA-S) displays a high dielectric constant up to ~160 with a peculiar temperature dependence [25] and enhanced ion-exchange selectivity to radio-active Cs^+ and Sr^{2+} [26–28].

Theoretically, S_3^- was considered in Refs. [29–33]. The calculations suggested the bond length r = 0.199–0.204 nm and the bond angle α = 114.7°-116.3° for free-standing S_3^- with the C_{2V} point group geometry (Fig. 1). Its three normal vibration modes (Fig. 1) are Raman active. The symmetric bond-stretching mode (A_1 symmetry) with a frequency ν_1 = 533-555 cm^{-1}, the bond-bending mode (A_1) with a frequency ν_2 = 232-269 cm^{-1} and anti-symmetric bond-stretching mode (B_2) with a frequency ν_3 = 569-590 cm^{-1} were experimentally observed in many works [2,3,6,7,10–13,15,20–22]. Depending on theoretical approach, calculated frequencies vary in wide intervals, namely ν_1 = 504-557

* Corresponding author.
** Corresponding author.
E-mail addresses: Vladimir.Poborchii@gmail.com (V.V. Poborchii), Andrei.Fotiadi@oulu.fi (A.A. Fotiadi).

https://doi.org/10.1016/j.matchemphys.2024.129103
Received 2 November 2023; Accepted 18 February 2024
Available online 21 February 2024

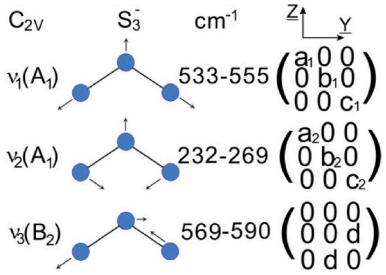

Fig. 1. Normal vibration modes of S_3^-. The mode symmetries are indicated on the left; the intervals of the experimentally observed frequencies are shown in the middle and the Raman activity tensors are displayed on the right.

cm^{-1}, ν_2 = 217-234 cm^{-1} and ν_3 = 531-599 cm^{-1} [30,31,33].

Previous optical studies of SOD-cage-confined S_3^- were done mostly on polycrystalline or powder samples with no attention to the light polarization. In contrast, here, we apply the method of polarization-orientation RS [34–36], an important alternative to the X-ray diffraction, for characterization of S_3^- confined in the SOD cages of LTA single crystals. This method can be easily applied for characterization of species confined in anisotropic zeolites like MOR, AFI, CAN and CHA [37–42] while it is always a challenge in case of cubic zeolites like LTA. Using this method, we determine orientation of the anions in LTA along with the S_3^- vibration mode Raman tensor calculations. We observe a record-high ν_2 ~ 274 cm^{-1} indicating the LTA-confined anion compression. The ν_2 high frequency leads to the Fermi-resonance of the $2\nu_2$ over-tone with the ν_1 mode. Interestingly, despite similarity of the polarization properties of ν_1 and ν_2 modes, polarization-orientation behavior of two Fermi-resonance bands appeared to be different. Additionally, anomalous S_3^- stretching mode frequency vs. temperature dependence is found and rather strong S_3^- luminescence is observed in the infrared (IR) spectral region. We discuss a role of S_3^- in the high dielectric constant up to ~160 and a possible contribution of the anion to the ion-exchange selectivity to Sr^{2+}/Cs^+ enhancements of LTA with sulfur.

2. Experimental and theoretical methods

Synthetic LTA zeolites ($Na_{12}Al_{12}Si_{12}O_{48}$) were used in this work. Crystal growth procedure is described in Ref. [43]. LTA has nearly spherical-shape large cavities with diameter of ~1.14 nm which are connected through narrow windows of ~0.42 nm diameter (Fig. 2). Each large cavity is accompanied by a small cavity, sodalite cage, with the diameter of ~0.63 nm. The zeolite structures are accessible at the International Zeolite Association website http://www.iza-structure.org/IZA-SC/ftc_table.php. The sizes of the cubic LTA crystals were ~20 μm along the edge of the cube.

Dehydration of zeolites in vacuum was performed in Pyrex ampoules for the sample LTA-S-300 at the temperature t ~300 °C and for the sample LTA-S-550 at t ~550 °C. The design of the ampoules made it possible to add sulfur powder to the zeolite after dehydration without exposing the dehydrated samples to air. The subsequent adsorption of the sulfur vapor was carried out at the same temperatures during a few days until the color of the sample was saturated: yellowish for LTA-S-300 and green for LTA-S-550. These two temperatures ~300 °C and ~550 °C, in accordance with previously obtained data, were chosen for the formation of solely S_8 rings in the LTA large cavities similar to Refs. [34,44] and for the maximal possible loading of LTA with sulfur via adsorption [20], respectively.

RS of the LTA-S-300 and LTA-S-550 single crystals were studied using Renishaw micro-Raman spectrometer with ~1 μm focused laser probe size. The 514.5 nm line of the Ar^+ laser and 633 nm line of the He–Ne laser were used for the RS excitation. Photoluminescence spectra were recorded using the same spectrometer. UV–visible OAS were studied using Carl Zeiss micro-optical spectrometer, the light probe size being ~5 μm. The samples were intentionally broken to minimize their optical density in the ultra-violet (UV) spectral range and placed into glycerol between two cover glasses to avoid surface light scattering.

The S_3^- Raman frequencies and intensities were calculated using the density functional theory (DFT). The DFT calculations were performed with the Turbomole 7.6 software package [45] using gradient PBE [46] and hybrid PBE0 [47] exchange-correlation functionals and def2-TZVP basis sets [48]. The cluster model, consisting of the whole SOD cage ($[S_3Na_8T_{12}O_6(OH)_{24}]^{5-}$), was cut from the periodic ultramarine model from Ref. [31], and the dangling bonds were saturated with H atoms. In order to get reasonable vibrational frequencies, cluster geometry was optimized. The positions of terminal H atoms were fixed during optimization, and their masses were set to large values (999 a. u.) to minimize the values of imaginary frequencies arising from constrained optimization (the frequencies were found to be below 10 cm^{-1}).

3. Optical absorption and Raman spectra of S_3^- confined in LTA single crystal

OAS of LTA-S-300 and LTA-S-550 single crystals are shown in Fig. 3 (a). Both samples display S_8 ring absorption band with a maximum at ~280–285 nm. Additionally, the S_3^- band at ~590 nm (~2.1 eV) is observed in the LTA-S-550 spectrum. This absorption band was attributed to the $^2B_1 \rightarrow {}^2A_2$ electron transition [29], which is allowed to the light polarization parallel to the **Y**-axis of the S_3^- molecule (Fig. 1).

Fig. 3(b–f) show RS of LTA-S-300(b) and LTA-S-550(b-f) single crystals at the temperatures of ~300 K and ~77 K with the excitation wavelengths λ = 514.5 nm and 632.8 nm. Polarization configurations

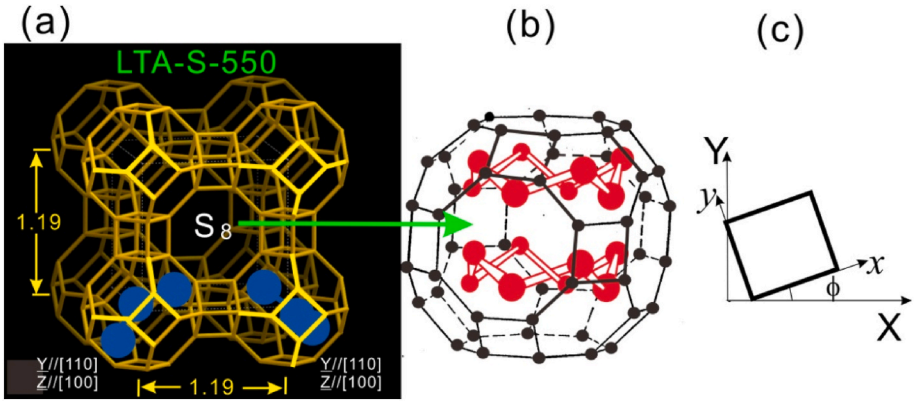

Fig. 2. Framework of LTA with S_3^- anions in the sodalite cages (a); S_8 double ring cluster in the LTA large cavity (b); schematic view of the LTA-S crystal rotated in the laboratory co-ordinate XY-plane (c).

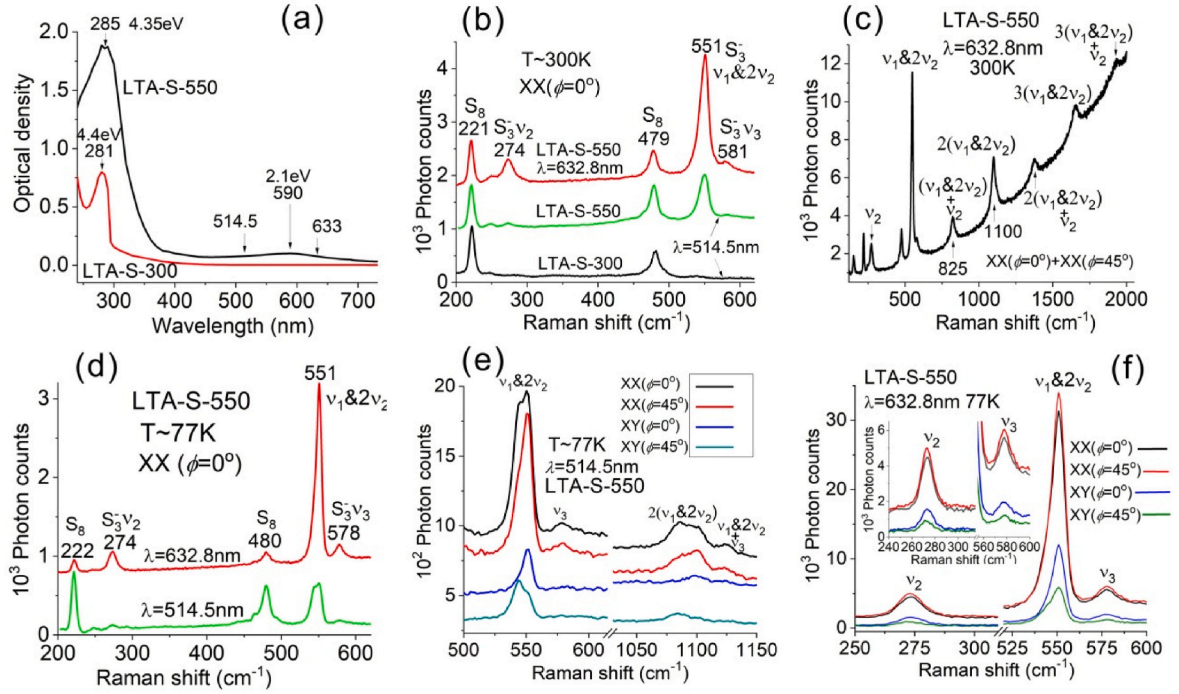

Fig. 3. OAS of LTA-S-300 and LTA-S-550 single crystals (a); RS of the same samples for the polarization configuration **XX**($\varphi = 0°$) (b); resonant RS of LTA-S-550 up to ~2000 cm^{-1} at $\lambda = 632.8$ nm (c); low-temperature ($T \sim 77$ K) RS of LTA-S-550 for **XX**($\varphi = 0°$) (d), for different configurations at $\lambda = 514.5$ nm (e) and $\lambda = 632.8$ nm (f).

XX and **XY** were used, the first/second index standing for the polarization of the incident/scattered light in the laboratory **X** and **Y** axes (Fig. 2(c)). The angle φ is the rotation angle of the LTA crystal in the **XY** plane (Fig. 2(c)).

RS of LTA-S-300 (Fig. 3(b), black curve) with the excitation wavelength $\lambda = 514.5$ nm displays only S_8 ring bands like in Ref. [34], where detailed RS polarization/orientation study showed that the rings are oriented by their 4-fold axis along the LTA 4-fold axis (Fig. 2 (b)) in agreement with the LTA-S single crystal X-ray diffraction study [43]. RS of LTA-S-550 (Fig. 3(b), green curve) displays same S_8 bands and an additional S_3^- band at ~551 cm^{-1}, other conditions being equal. With the excitation wavelength $\lambda = 632.8$ nm (Fig. 3(b), red curve), the S_3^- band at ~551 cm^{-1} is enhanced compared to the S_8 bands. Additionally, two other S_3^- characteristic bands at ~274 cm^{-1} (ν_2) and ~581 cm^{-1} (ν_3) become clearly recognized. Similar resonance Raman enhancement of the S_3^- bands due to the $^2B_1 \rightarrow {}^2A_2$ electron transition was observed earlier in Refs. [2,3,13]. A number of the S_3^- overtones due to the resonance RS at the 632.8 nm excitation are shown in Fig. 3(c). Importantly, the record-high ν_2 frequency of ~274 cm^{-1} is a clear indication of a strong anion compression in the SOD cavity. Appearance of S_3^- in LTA at the elevated sulfur adsorption temperature is associated with an increase in the S_2 and S_3 molecule concentration in the sulfur vapor on one hand and with the enlargement of the SOD cage vibration amplitude on the other hand, which is similar to the appearance of SOD-cage-confined Se_2^- in LTA [36].

Although it looks like the ~551 cm^{-1} band should be assigned to the ν_1 mode, it is, actually, a doublet ν_+ due to the Fermi resonance of the ν_1 mode with the $2\nu_2$ overtone. Its doublet structure is clearly seen at the temperature $T \sim 77$ K and $\lambda = 514.5$ nm in the range of ν_+ and $2\nu_+$ modes (Fig. 3(d and e)).

A few important findings can be observed in the low-temperature RS, namely: a strong enhancement of the S_3^- bands compared to the S_8 bands at $\lambda = 632.8$ nm and an anomalous downshift of the anti-symmetric bond-stretching mode ν_3 from ~581 cm^{-1} to ~578 cm^{-1} in contrast to the regular slight upshifts of the S_8 bands (Fig. 3(d), red curve). The effects can be explained by a zeolite-induced tensile strain of the anion at low temperatures. However, since the molecule is compressed in the SOD cage, we can attribute the effect to a partial compressive stress relaxation of the anion with a decrease in temperature, as was suggested in Ref. [36] in case of LTA-confined Se_2^-. Anyway, it is clear that the anion bond lengths appeared to be enlarged when the temperature was decreased, which is anomalous. Interestingly, the bond angle seems to remain unchanged with cooling since the bond-bending mode frequency is the same ν_2 ~274 cm^{-1} with ~0.5 cm^{-1} accuracy at both T ~300 K and ~77 K. Raman enhancement of S_3^- bands at T ~77 K is associated with a red shift of the ~590 nm absorption band due to the anion bond length enlargement, which is improving the resonance Raman condition for the $\lambda = 632.8$ nm excitation similar to the improvement of the resonance condition of the Se_2^- band and the 514.5 nm excitation wavelength at T ~77 K [36].

4. Fermi resonance, luminescence, polarization-orientation Raman spectra dependencies of S_3^- and understanding high dielectric constant of LTA-S

Using polarization-orientation RS method [34–36], one can find that the behavior of two components of the ~551 cm^{-1} band is different (Fig. 3(e)). Indeed, the low-frequency component nearly completely vanishes at the polarization configuration **XY**($\varphi = 0°$) while the high-frequency one remains relatively strong at this configuration and minimizes at **XY**($\varphi = 45°$). Polarization/orientation dependence of the bond-bending mode ν_2 at ~274 cm^{-1} (Fig. 3(f)) is similar to that of the doublet high-frequency component. Fig. 4(a–d) show Lorentz fitting of the Fermi-resonance doublet. Theoretically polarization-orientation dependence of the band intensities is considered in the following paragraph.

The Raman scattering efficiency of a vibration mode of crystal for the incident and scattered photons with polarizations in the directions of unit vectors $\mathbf{e}_I$ and $\mathbf{e}_S$, respectively, is given by a general expression [49]:

$$R_{IS} = K(\Sigma e_I^{\sigma} A_{\sigma\rho} e_S^{\rho})^2 \quad (1)$$

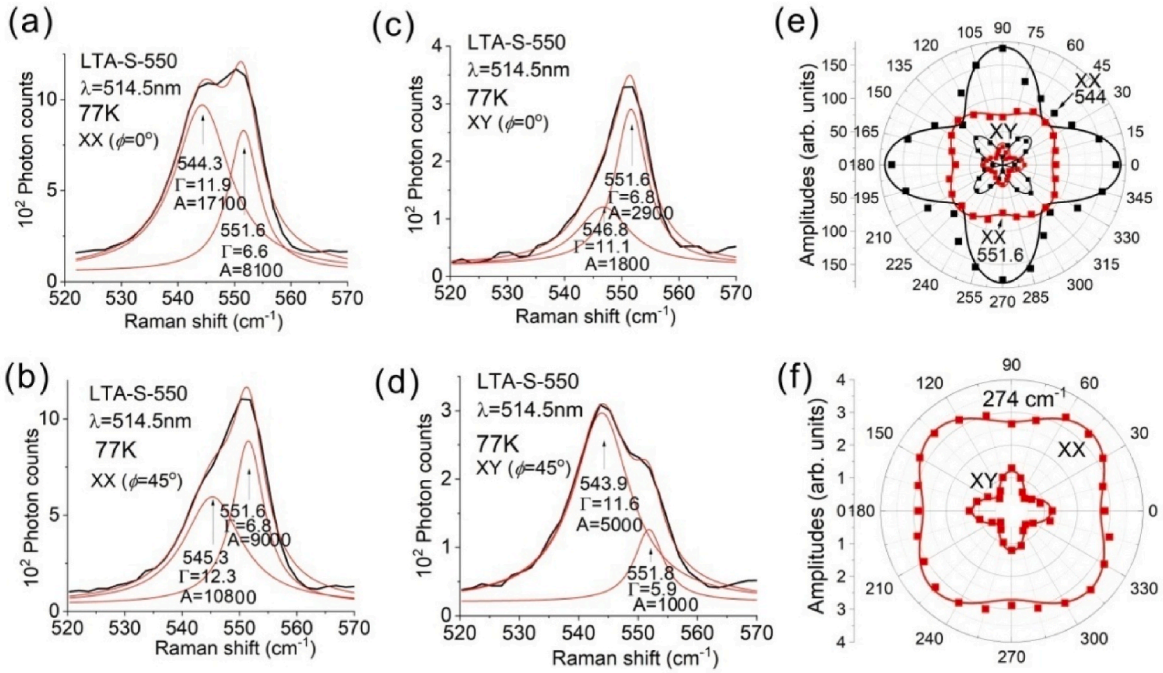

Fig. 4. Fitting of LTA-S-550 RS (λ = 514.5 nm) in the S_3^- bond-stretching mode region as a summation of two Lorentzians in the form $(2A/\pi)(\Gamma/(4(\nu-\nu_0)^2 + \Gamma^2))$ with the peak frequencyν_0, amplitude A and half-width Γ for **XX**($\varphi = 0°$) (a), **XX**($\varphi = 45°$) (b), **XY**($\varphi = 0°$) (c) and **XY**($\varphi = 45°$) (d); angular dependencies of the low-frequency (black squares) and high-frequency (red squares) peak amplitudes for **XX** and **XY** configurations with theoretical curves shown in corresponding colours (e); angular dependence of the 274 cm^{-1} peak amplitude (red squares) with red theoretical curve (f). (For interpretation of the references to color in this figure legend, the reader is referred to the Web version of this article.)

where K is a constant of proportionality, $A_{\sigma\rho}$ is the Raman tensor corresponding to the studied vibration, and e_I^σ and e_S^ρ are components of the unit vectors along the principal axes of a crystal. Formula (1) is obviously valid for the Raman efficiency of vibrations of species incorporated into zeolite crystals as well as for the Raman efficiency of vibrations of crystals. However, for the zeolite-confined species, e_I^σ and e_S^ρ are components of the unit vectors along the principal axes of the species instead of the principal axes of crystals.

Let us consider S_3^- located in the (110) plane of LTA with the molecule Y-axis oriented along the **[110]** direction of the crystal and the Z-axis oriented along the **[100]** direction of the crystal. Raman tensors of both symmetric stretching and bending A_1 modes have non-zero diagonal components a, b and c (Fig. 1). Judging from the atomic displacements only in the Y Z plane, we neglect a. We focus on the cases: 1) $b^2 \gg c^2$ and 2) $c^2 \gg b^2$. According to formula (1), we obtain for the first case:

$$R_{XX} = b^2(cos^4(\varphi\ -45°) + sin^4(\varphi\ -45°)+(cos^4\varphi + sin^4\varphi)/2) \quad (2)$$

$$R_{XY} = b^2(2cos^2(\varphi\ -45°)sin^2(\varphi\ -45°) + cos^2\varphi\ sin^2\varphi) \quad (3)$$

and for the second case:

$$R_{XX} = 2c^2(cos^4\varphi + sin^4\varphi) \quad (4)$$

$$R_{XY} = 4c^2cos^2\varphi\ sin^2\varphi \quad (5)$$

For $b^2 \gg c^2$, R_{XX}/R_{XY} displays máxima/minima at $\varphi = 45°$, 135°, 225° and 315° while minima/maxima at 0°, 90°, 180° and 270°. It is vice versa for $c^2 \gg b^2$. Fig. 4(e) shows experimental (symbols) and theoretical (curves) angle dependences of the intensities of the low-frequency (black) and high-frequency (red) components of the S_3^- Fermi-resonance. The low-frequency component intensity is perfectly described by equations (4) and (5) for **XX** and **XY** polarization configurations, respectively (black curves), which corresponds to $c^2 \gg b^2$. The high-frequency component intensity angular dependence is described by equation (3) for **XX**-configuration and (4) for **XY**-configuration, which corresponds to $b^2 \gg c^2$. The angular dependence of the Raman intensity of the high-frequency component of the Fermi resonance coincides with that of the 274 cm^{-1} bending mode (Fig. 4(f)).

Theoretically, Raman tensor components a_1, b_1, c_1 and a_2, b_2, c_2 of the ν_1 and ν_2 modes, respectively (Fig. 1), can be calculated using time-dependent density functional theory [50], which is included to the Turbomole package [45]. For a free standing S_3^- and off-resonance excitation, we obtained $a_1 \sim 2.06$, $b_1 \sim 63.2$, $c_1 \sim 14.1$ and $a_2 \sim 0.56$, $b_2 \sim 21.9$, $c_2 \sim -8.1$. In accordance with our assumption, a components appeared to be small compared to b and c ones, while $b_1^2 \sim 20c_1^2$ and $b_2^2 \sim 7.3c_2^2$. For the resonance excitation, close to the electron transition $^2B_1 \rightarrow {}^2A_2$, the domination of b over c components becomes even stronger due to the B_2 symmetry of the transition allowed for the electric field of light $\boldsymbol{E}$//Y. (To be correct, Raman intensity values, obtained for the resonance excitation cannot be considered as enough accurate.) Thus, this theoretical consideration suggests that the condition $b^2 \gg c^2$ works for both ν_1 and ν_2 modes.

At the first glance, the validity of the condition $b^2 \gg c^2$ for both ν_1 and ν_2 modes seems contradicting to our experimental observation suggesting different polarization/orientation behavior for the bending and Fermi-resonance high-frequency ν_+ modes with $b^2 \gg c^2$ on one hand and the low-frequency ν_- mode of the Fermi resonance with $c^2 \gg b^2$ on the other hand. However, actually, there is no contradiction since the Fermi-resonance modes are mixed. Theoretical consideration is valid for the non-mixed bending mode. For the mixed modes, we have to apply our theoretical single ν_1 mode result to the total Raman intensity of the Fermi-resonance doublet, which is mainly determined by its high-frequency ν_+ component at the resonant 632.8 nm excitation (Fig. 3 (f)). This component polarization/orientation behavior is similar to that of the bending mode Fig. 4(e and f)) and corresponds to $b^2 \gg c^2$ and orientation of the S_3^- molecule by its Y and Z axes along the **[110]** and **[100]** LTA directions, respectively. Lorentz curve fitting of the Fermi doublet at the 632.8 nm excitation is shown in Fig. 5(a) and the band Lorentz amplitudes compared to that of the ~480 cm^{-1} band of S_8, which are proportional to the areas under curves, vs. wavelength are

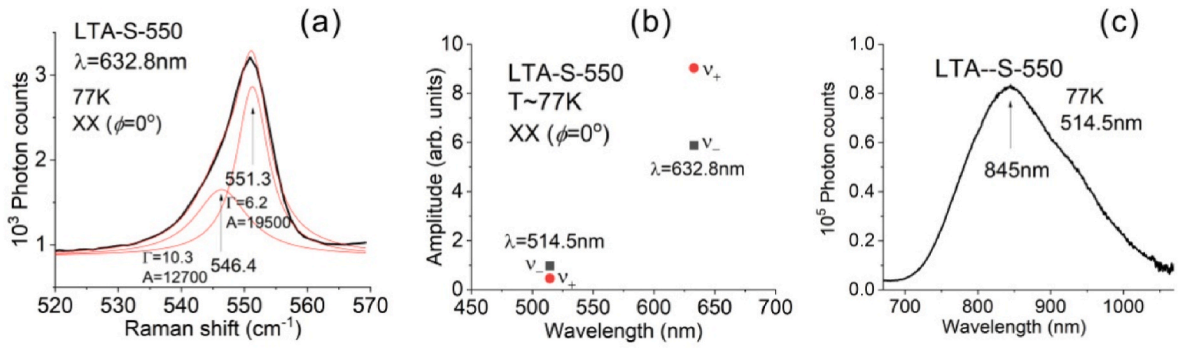

Fig. 5. Fitting of the $\nu_{\pm}$ bands at $\lambda = 632.8$ nm (a); ratios of the Lorentz amplitudes of the $\nu_{\pm}$ bands to that of the 480 cm^{-1} band of S_8 (b); luminescence spectrum of LTA-S-550 (c).

shown in Fig. 5(b). Apparently, the ν_+ band is enhanced compared the ν_- band at the 632.8 nm resonant excitation.

It would be important to determine a real value of ν_1 of S_3^- in LTA. As was shown nearly 100 years ago [51,52], the Fermi-resonance component frequencies can be expressed by the equation, which is slightly modified for our particular case:

$$\nu_{\pm} = (\nu_1+2\nu_2)/2 \pm [4W^2 + (\nu_1 - 2\nu_2)^2]^{1/2}/2 \quad (6)$$

where ν_1 and ν_2 are unperturbed frequencies while W is perturbation energy in cm^{-1} given by the anharmonic terms in the interatomic potential. The unperturbed $2\nu_2 \sim 2 \times 274 = 548$ cm^{-1} with $\nu_+ \sim 551.6$ cm^{-1} and $\nu_- \sim 544$ cm^{-1} at $T \sim 77$ K. The ν_+ value is rather accurately determined using the Lorentz curve fitting (Fig. 4(a–d)). The ν_- value is less accurate. Lorentz fitting results suggest the low-frequency component peak in the range 543.9–546.8 cm^{-1}. The value of ~ 544 cm^{-1} seems to be most precise since the Lorentz bands centered at ~ 544.3 cm^{-1} (Fig. 4(a)) and 543.9 cm^{-1} (Fig. 4(d)) are relatively strong and their positions are rather accurately determined. Similar Lorentz fitting of LTA-S-550 room-temperature RS reveals ~ 545 cm^{-1} value for ν_-, which correlates with the anomalous temperature-induced shift of ν_3. At the same time, $\nu_+ \sim 551.6$ cm^{-1} appeared to be nearly independent off the temperature like $\nu_2 \sim 274$ cm^{-1} suggesting that, in the sense of the frequency, ν_+ mainly originates from $2\nu_2$ while ν_- from ν_1 with the Raman activity of both ν_+ and ν_- originating from that of ν_1. Briefly, $2\nu_2$ mode borrowed its high Raman activity from the ν_1 mode, which is rather common for Fermi-resonances [52].

We can roughly estimate ν_1, $\nu_{av} = (\nu_1+2\nu_2)/2 \sim (\nu_+ + \nu_-)/2$ and W. Indeed, $\nu_{av} \sim 547.8$ cm^{-1} for $T \sim 77$ K with $\nu_1 \sim 547.6$ cm^{-1} and $W \sim 3.6$ cm^{-1}. Of course, these values cannot be precisely determined since the frequency measurement accuracy is ~ 0.5 cm^{-1}. Nevertheless, we can conclude that the ν_1, and $2\nu_2$ frequencies nearly coincide with each other and the perturbation energy is in the range of 3–4 cm^{-1}. For future references, we postulate $\nu_1 \sim 547.5$ cm^{-1} at $T \sim 77$ K and $\nu_1 \sim 548.5$ cm^{-1} at $T \sim 300$ K.

Interestingly the ratio $W/\nu_{av} \sim 0.5\%$ for S_3^- looks very low compared to those of the very famous Fermi-resonance molecules CO_2 and CS_2, which can be easily calculated from the data of Ref. [53]. The ratios are $\sim 3.7\%$ for CO_2 and $\sim 6.5\%$ for CS_2 in the gas state at $T \sim 300$ K and not much depending on T, namely, they are $\sim 3.5\%$ and $\sim 4\%$ for solid CO_2 and CS_2, respectively, at $T \sim 100$ K. This is an indication of a very low anharmonicity of the S_3^- vibrations compared to those of CO_2 and CS_2.

Table 1 shows experimental and theoretical S_3^- Raman frequencies and absorption band wavelengths. As we mentioned, $\nu_2 = 274$ cm^{-1} is the record-high S_3^- bond-bending mode frequency observed in any environment, which is indicating the strongest S_3^- bond angle contraction in the SOD cage of LTA. From Table 1 data, it is clear that both ν_1 and ν_2 of SOD-cage-confined S_3^- are significantly higher than those of S_3^- in liquid solutions. A large deviation in the ν_1 ($\sim 5\%$) and ν_2 ($\sim 15\%$) values is a result of such a compression, bond angle being a softer parameter than the bond length. The absorption wavelength of the compressed SOD-cage-confined S_3^- is shorter than that of S_3^- in liquid solutions.

Table 1
S_3^- Raman frequencies and absorption band wavelengths.

	ν_1 (cm^{-1})	ν_2 (cm^{-1})	ν_3 (cm^{-1})	λ (nm)	references
LTA-S-550 T–300K	548.5	274	581	590	this work
S_3^- in SOD cages	545–555	258–269	580–590	590-610	[1–4,6,7,13,15,20–22]
S_3^- in liquid solutions	533–535	232–235	571	610-620	[3,10–13]
free S_3^- theory PBE0	553.1	233.4	597.6		this work
free S_3^- theory PBE	513.1	218.5	547.9		this work
S_3^- in-cage PBE	536.2	254.6	562.7		this work

Our theoretical calculations confirm the S_3^- compression in the SOD cage. DFT calculations at the PBE level give higher frequencies for S_3^- inserted into the cage ($S_3Na_8T_{12}O_6(OH)_{24}$ cluster with T = Si or Al) than those of free-standing S_3^-. More detailed calculations considering S_3^- environment were performed in Ref. [33]. It was shown that the bond length $r \sim 0.2012$ nm and bond angle $\alpha \sim 116.33°$ of free-standing S_3^- were $\sim 1\%$ and $\sim 5\%$, respectively, decreased in clusters.

As we mentioned in previous sections, the S_3^- compression in SOD cages is similar to that found for Se_2^- [36]. The compression of the SOD-confined Se_2^- was clearly demonstrated via comparison with the cancrinite-channel-confined Se_2^-, which is not compressed in the channel direction [40]. Interestingly, the compression of Se_2^- in SOD cages of LTA was found to be weaker than that in SOD cages of SOD. Here, we observe an opposite in sense of the angle contraction. Se_2^- luminescence band wavelength was found to be dependent on the anion compression with the stronger compression corresponding to the shorter luminescence wavelength. We could not find any data on S_3^- luminescence in literature but we observe rather bright luminescence band of LTA-S-550 with a maximum at ~ 845 nm here and assign it to S_3^- (Fig. 5(c)). Its strong intensity can be associated with the anion compression.

Finally, we should note that the high dielectric constant $\varepsilon \sim 160$ of LTA-S, attributed to the temperature-activated dipoles [25], is most probably associated with a high concentration of S_3^- anions. Indeed, LTA-S-550 density measurement using single crystal flotation in Clerici solutions [54] gave the value of the sulfur loading density $\sim 20 \pm 2$ atoms per a simplified LTA unit cell (large cavity + sodalite cage), which corresponds well to 16 atoms in the large cavity plus 3 atoms in the sodalite cage. Neutral non-polar S_8 rings are unable producing any ε enhancement of LTA. Contrary, S_3^- has both charge and dipole moment which are able to make the ε enhancement.

Our LTA-S-550 RS suggest a very little change in S_8 properties with

temperature, namely, just usual slight expansion/contraction, which is consistent with a weak van der Waals interaction between the rings and LTA. In contrast, the (110) plane location of S_3^- in sodalite cages, observed here, can be associated with a strong interaction of its terminal atoms with Na^+ cations in the LTA 6-membered rings. The interaction is rather strong, at low temperatures. Our RS and published earlier EPR data [20,24] confirm that. Anomalous expansion of the S_3^- bond-lengths with a decrease in temperature observed here is a clear indication of the strong anion-cation interaction. This corresponds to relatively low $\varepsilon \sim 10$ for $T < 200$ K [25]. However, S_3^- mobility increases with the temperature, which enlarges S–Na atomic distances and decreases S_3^- bond-lengths. Importantly, the increase in the S_3^- mobility enhances polarizability of the system organized by the positively charged LTA and negatively charged S_3^- anions. S_3^- dipole moment can also contribute to this. The maximal LTA-S $\varepsilon \sim 160$ was observed at T ~374 K.

The fact that the (110) plane location of S_3^- in the sodalite cage is associated with a strong interaction of its terminal atoms with Na^+ cations in the LTA 6-membered rings can explain a strong influence of the sulfur doping on the LTA cation exchange to radioactive Sr^{2+} and Cs^+ [26,27].

5. Conclusions

We applied polarization-orientation RS to trisulfur radical anions S_3^- formed in SOD cages of zeolite LTA single crystals. This method is shown to be a fruitful alternative to XRD since it does not require large zeolite crystals or high occupancy factors. We showed that the anions are located in the (110) plane of LTA and oriented by their two-fold axes along the LTA four-fold axes. The record-high bond-bending mode frequency $\nu_2 \sim 274$ cm^{-1} of S_3^- suggests a strong bond angle contraction in SOD cages of LTA. A Fermi resonance of the $2\nu_2$ overtone with the ν_1 symmetric bond-stretching mode is clearly displayed in the 544-552 cm^{-1} frequency range. Despite similarity of the polarization properties of ν_1 and ν_2 modes, the polarization-orientation behavior of two Fermi-resonance bands ν_+ and ν_- appeared to be different suggesting that their Raman tensor components are significantly different. This difference can be associated with a contribution of electron transitions with wavelengths shorter than 590 nm, which could become noticeable due to the anion compression and, possibly, symmetry reduction. Additionally, an anomalous S_3^- stretching mode frequency vs. temperature dependence is found and rather strong S_3^- luminescence is observed in the near IR spectral region with a maximum at ~845 nm. And importantly, we can now explain the unusually high $\varepsilon \sim 160$ of LTA-S due to the understanding of the role of S_3^- anions, their location, orientation and interaction with Na^+ cations.

Declaration of competing interest

There is no conflict of interests.

Data availability

Data will be made available on request.

Acknowledgements

The authors are grateful to D. Rappoport for useful comments regarding the Turbomole software operation. The work of I. Glukhov was supported by the Ministry of Science and Higher Education of the Russian Federation (project FEUF-2023-0003). A. Fotiadi was supported by the European Union's Horizon 2020 research and innovation programme (Individual Fellowship, H2020-MSCA–IF–2020, #101028712).

References

[1] U. Hofmann, E. Herzenstiel, E. Schonemann, K.-H. Schwarz, Ultramarin, Z. Anorg, Allg. Chem. 367 (1969) 119–129, https://doi.org/10.1002/zaac.19693670303.
[2] R.J.H. Clark, M.L. Franks, The resonance Raman spectrum of ultramarine blue, Chem. Phys. Lett. 34 (1975) 69–72, https://doi.org/10.1016/0009-2614(75)80202-8.
[3] B. Lede, A. Demortier, N. Gobeltz-Hautecoeur, J.-P. Lelieur, E. Picquenard, C. Duhayon, Observation of the ν_3 Raman band of S_3^- inserted into sodalite cages, J. Raman Spectrosc. 38 (2007) 1461–1468, https://doi.org/10.1002/jrs.1795.
[4] D. Reinen, G.-G. Lindner, The nature of the chalcogen colour centres in ultramarine-type Solids, Chem. Soc. Rev. 28 (1999) 75–84, https://doi.org/10.1039/A704920J.
[5] S.D. McLaughlan, D.J. Marshall, Paramagnetic resonance of sulfur radicals in synthetic sodalites, J. Phys. Chem. 74 (1970) 1359–1363, https://doi.org/10.1021/j100701a035.
[6] M. Gonzalez-Cabrera, P. Arjonilla, A. Domínguez-Vidal, M.J. Ayora-Canada, Natural or synthetic? Simultaneous Raman/luminescence hyperspectral microimaging for the fast distinction of ultramarine pigments, Dyes Pigments 178 (2020) 108349, https://doi.org/10.1016/j.dyepig.2020.108349.
[7] G.D. Ventura, F. Capitelli, M. Sbroscia, A. Sodo, A Raman study of chalcogen species in sodalite-group minerals from the volcanic rocks of Latium (Italy), J. Raman Spectrosc. 51 (2020) 1513–1521, https://doi.org/10.1002/jrs.5665.
[8] T. Chivers, The blue chromophore in sulphur-doped borate glasses (boro-ultramarine), J. Mater. Sci. 12 (1977) 417–418, https://doi.org/10.1007/BF00566287.
[9] T. Chivers, E. Gilmour, R.A. Kydd, Vibrational spectra of sulpur-doped borate glasses, J. Mater. Sci. 13 (1978) 1585–1588, https://doi.org/10.1007/BF00553216.
[10] T. Chivers, I. Drummond, Characterization of the trisulfur radical anion S_3^- in blue solutions of alkali polysulfides in hexamethylphosphoramide, Inorg. Chem. 11 (1972) 2525–2527, https://doi.org/10.1021/ic50116a047.
[11] F.P. Daly, C.W. Brown, Raman spectra of sulfur dissolved in primary amines, J. Phys. Chem. 77 (1973) 1859–1861, https://doi.org/10.1021/j100634a008.
[12] T. Chivers, C. Lau, Raman spectroscopic identification of the S_4N^- and S_3^- ions in blue solutions of sulfur in liquid ammonia, Inorg. Chem. 21 (1982) 453–455, https://doi.org/10.1021/ic00131a089.
[13] R.J.H. Clark, D.G. Cobbold, Characterization of sulfur radical anions in solutions of alkali polysulfides in dimethylformamide and hexamethylphosphoramide and in the solid state in ultramarine blue, green, and red, Inorg. Chem. 17 (1978) 3169–3174, https://doi.org/10.1021/ic50189a042.
[14] T. Chivers, P.J.W. Elder, Ubiquitous trisulfur radical anion: fundamentals and applications in materials science, electrochemistry, analytical chemistry and geochemistry, Chem. Soc. Rev. 42 (2013) 5996–6005, https://doi.org/10.1039/c3cs60119f.
[15] W. Holzer, W.F. Murphy, H.J. Bernstein, Raman spectra of negative molecular ions doped in alkali halide crystals, J. Mol. Spectrosc. 32 (1969) 13–23, https://doi.org/10.1016/0022-2852(69)90139-8.
[16] G.S. Pokrovski, L.S. Dubrovinsky, The S_3^- ion is stable in geological fluids at elevated temperatures and pressures, Science 331 (2011) 1052–1054, https://doi.org/10.1126/science.1199911.
[17] R. Steudel, T. Chivers, The role of polysulfide dianions and radical anions in the chemical, physical and biological sciences,including sulfur-based batteries, Chem. Soc. Rev. 48 (2019) 3279–3319, https://doi.org/10.1039/C8CS00826D.
[18] T. Chivers, Ubiquitous trisulphur radical ion S3-, Nature 252 (1974) 32–33, https://doi.org/10.1038/252032a0.
[19] D. Arieli, D.E.W. Vaughan, D. Goldfarb, New synthesis and insight into the structure of blue ultramarine pigments, J. Am. Chem. Soc. 126 (2004) 5776–5788, https://doi.org/10.1021/ja0320121.
[20] V.N. Bogomolov, V.P. Petranovskii, V.V. Poborchii, S.V. Kholodkevich, Absorption, Raman and ESR spectra and the dielectric permittivity of NaA-S cluster crystals, Sov. Phys. Solid State 25 (1983) 1415–1417.
[21] S.K. Hoffmann, J. Goslar, S. Lijewski, I. Olejniczak, A. Jankowska, A. Werbinska, S. Kowalak, Sulfur pigments synthesized from zeolite LTA under vacuum and in air. XRD and spectroscopic (UV-vis, FTIR, Raman, ESR, ESE) characterization, Ind. Eng. Chem. Res. 49 (2010) 8192–8199, https://doi.org/10.1021/ie100983m.
[22] S.K. Hoffmann, J. Goslar, S. Lijewski, I. Olejniczak, A. Jankowska, S. Zeidler, N. Koperska, S. Kowalak, S_3^- radicals in ε-cages of cancrinite and zeolite L: spectroscopic and magnetic resonance studies, Microporous Mesoporous Mater. 151 (2012) 70–78, https://doi.org/10.1016/j.micromeso.2011.11.014.
[23] S. Kowalak, A. Jankowska, Application of zeolites as matrices for pigments *Micropor*, Mesopor. Mater. 61 (2003) 213–222, https://doi.org/10.1016/S1387-1811(03)00370-6.
[24] J. Goslar, S. Lijewski, S.K. Hoffmann, A. Jankowska, S. Kowalak, Structure and dynamics of S3− radicals in ultramarine-type pigment based on zeolite A: electron spin resonance and electron spin echo studies, J. Chem. Phys. 130 (2009) 204504, https://doi.org/10.1063/1.3124551.
[25] V.N. Bogomolov, E.K. Kudinov, T.M. Pavlova, V.P. Petranovskii, Occurrence of large temperature-activated dipole moments of sulfur clusters in zeolite inclusions, JETP Lett. 30 (1979) 382–384.
[26] H.-M. Yang, H. Jeon, Y. Lee, M. Choi, Sulfur-modified zeolite A as a low-cost strontium remover with improved selectivity for radioactive strontium, Chemosphere 299 (2022) 134309, https://doi.org/10.1016/j.chemosphere.2022.134309.
[27] E. Han, Y.-G. Kim, H.-M. Yang, I.-H. Yoon, M. Choi, Synergy between zeolite framework and encapsulated sulfur for enhanced ion-exchange selectivity to

radioactive cesium, Chem. Mater. 30 (2018) 5777–5785, https://doi.org/10.1021/acs.chemmater.8b02782.
[28] H.-M. Yang, C.W. Park, I. Kim, I.-H. Yoon, Y. Sihn, Sulfur-modified chabazite as a low-cost ion exchanger for the highly selective and simultaneous removal of cesium and strontium, Appl. Surf. Sci. 536 (2021) 147776, https://doi.org/10.1016/j.apsusc.2020.147776.
[29] W. Koch, J. Natterer, C. Heinemann, Quantum chemical study on the equilibrium geometries of S3 and S3-,The electron affinity of S_3 and the low lying electronic states of S_3^-, J. Chem. Phys. 102 (1995), https://doi.org/10.1063/1.469350, 6159-6157.
[30] R. Linguerri, N. Komiha, J. Fabian, P. Rosmus, Electronic states of the ultramarine chromophore S_3^-, Z. Phys. Chem. 222 (2008) 163–176, https://doi.org/10.1524/zpch.2008.222.1.163.
[31] J.A. Tossell, Calculation of the properties of the S3- radical anion and its complexes with Cu+ in aqueous solution, Geochem. Cosmochim. Acta 95 (2012) 79–92, https://doi.org/10.1016/j.gca.2012.07.020.
[32] J. Fabian, N. Komiha, R. Linguerri, P. Rosmus, The absorption wavelengths of sulfur chromophors of ultramarines calculated by time-dependent density functional theory, J. Mol. Struct.: THEOCHEM 801 (2006) 63–69, https://doi.org/10.1016/j.theochem.2006.08.050.
[33] P. Rejmak, Structural, optical and magnetic properties of ultramarine pigments: a DFT insight, J. Phys. Chem. C 122 (2018) 29338–29349, https://doi.org/10.1021/acs.jpcc.8b09856.
[34] V.V. Poborchii, Raman microprobe polarization measurements as a tool for studying the structure and orientation of molecules and clusters incorporated into cubic zeolites: S_8 and Se_{12} rings in zeolite A, J. Chem. Phys. 114 (2001) 2707–2717, https://doi.org/10.1063/1.1339268.
[35] V.V. Poborchii, A.V. Fokin, Raman and optical absorption spectra of oriented Se_8 and Se_{12} rings formed in zeolites: dependence on the Se loading density, Microporous Mesoporous Mater. 338 (2022) 111954, https://doi.org/10.1016/j.micromeso.2022.111954.
[36] V.V. Poborchii, V.P. Petranovskii, I.A. Glukhov, A.A. Fotiadi, Optical study of oriented double-Se8-ring clusters and luminescent Se_2^- anions in LTA at extremely high selenium loading density, Microporous Mesoporous Mater. 348 (2023) 112395, https://doi.org/10.1016/j.micromeso.2022.112395.
[37] V.V. Poborchii, Polarized Raman and optical absorption spectra of the mordenite single crystals containing sulphur, selenium or tellurium confined in the one-dimensional nanochannels, Chem. Phys. Lett. 251 (1996) 230–234, https://doi.org/10.1016/0009-2614(96)00045-0.
[38] V.V. Poborchii, A.V. Kolobov, J. Caro, V.V. Zhuravlev, K. Tanaka, Polarized Raman spectra of selenium species confined in nanochannels of $AlPO_4$ -5 single crystals, Chem. Phys. Lett. 280 (1997) 17–23, https://doi.org/10.1016/S0009-2614(97)01087-7.
[39] V.V. Poborchii, Oriented Se_6 ring clusters in zeolite single crystals: polarized Raman microscopy, optical absorption spectra and photo-induced effects, Microporous Mesoporous Mater. 308 (2020) 110559, https://doi.org/10.1016/j.micromeso.2020.110559.
[40] V.V. Poborchii, G.-G. Lindner, M. Sato, Selenium dimers and linear chains in one-dimensional cancrinite nanochannels: structure, dynamics, and optical properties, J. Chem. Phys. 116 (2002) 2609–2617, https://doi.org/10.1063/1.1434950.
[41] V.V. Poborchii, A.V. Fokin, A.A. Shklyaev, Optical properties of extreme tellurium nanowires formed in subnanometer-diameter channels, Nanoscale Adv. 5 (2023) 220–227, https://doi.org/10.1039/d2na00590e.
[42] V.V. Poborchii, A.V. Kolobov, J. Caro, V.V. Zhuravlev, K. Tanaka, Dynamics of single selenium chains confined in one-dimensional nanochannels of AlPO4-5: temperature dependencies of the first- and second-order Raman spectra, Phys. Rev. Lett. 82 (1999) 1955–1958, https://doi.org/10.1103/PhysRevLett.82.1955.
[43] V.P. Petranovskii, Y. Kiyozumi, N. Kikuchi, H. Hayamisu, Y. Sugi, F. Mizukami, The influence of mixed organic additives on the zeolite A and X crystal growth, Stud. Surf. Sci. Catal. 105 (1997) 149–156.
[44] K. Seff, The crystal structure of a sulfur sorption complex of zeolite 4A, J. Phys. Chem. 76 (1972) 2601–2605, https://doi.org/10.1021/j100662a023.
[45] S.G. Balasubramani, et al., TURBOMOLE: modular program suite for *ab initio* quantum-chemical and condensedmatter simulations, J. Chem. Phys. 152 (2020) 184107, https://doi.org/10.1063/5.0004635.
[46] J.P. Perdew, K. Burke, M. Ernzerhof, Generalized gradient approximation made simple, Phys. Rev. Lett. 77 (1996) 3865–3868, https://doi.org/10.1103/PhysRevLett.77.3865.
[47] J.P. Perdew, M. Ernzerhof, K. Burke, Rationale for mixing exact exchange with density functional approximations, J. Chem. Phys. 105 (1996) 9982–9985, https://doi.org/10.1063/1.472933.
[48] F. Weigend, R. Ahlrichs, Balanced basis sets of split valence, triple zeta valence and quadruple zeta valence quality for H to Rn: design and assessment of accuracy, Phys. Chem. Chem. Phys. 7 (2005) 3297–3305, https://doi.org/10.1039/B508541A.
[49] R. Loudon, The Raman effect in crystals, Adv. Phys. 13 (1964) 423–482, https://doi.org/10.1080/00018736400101051.
[50] D. Rappoport, F. Furche, Lagrangian approach to molecular vibrational Raman intensities using time-dependent hybrid density functional theory, J. Chem. Phys. 126 (2007) 201104, https://doi.org/10.1063/1.2744026.
[51] E. Fermi, On the Raman effect in carbon dioxide, Z. Phys. 71 (1931) 250–259, https://doi.org/10.1007/BF01341712.
[52] G. Herzberg, Infrared and Raman Spectra of Polyatomic Molecules, Van Nostrand Co, New York, 1945.
[53] K.D. Bier, H.J. Jodl, Tuning of the Fermi resonance of CO_2 and CS_2 by temperature, pressure and matrix material, J. Chem. Phys. 86 (1987) 4406–4410, https://doi.org/10.1063/1.452711.
[54] R.H. Jahns, Clerici solution for the specific gravity determination of small mineral grains, Am. Mineral. 24 (1939) 116–122.